This does not exclude the possibility that larger structural fragments (such as tetramers and pentamers) can also contribute to the low-frequency vibrational spectrum around the boson peak.

On the basis of these results, the following model of the glass transition of glycerol can be proposed. At temperatures far above T_g (186 K), the lifetime of the MRO or the cyclic glycerol trimer is expected to be too short to be underdamped on the time scale of the boson peak frequency ($\sim 10^{-12}$ s), and therefore only relaxation processes contribute to the dynamics of the system. As the system is cooled, the thermal excitation of atoms is suppressed, and, accordingly, the atoms in the MRO undergo collective motions on the time scale of low-frequency vibrations to yield a boson peak. In other words, a transition from relaxational (overdamped) to vibrational (underdamped) collective molecular motion occurs.

According to MCT, a blocking of the viscous flow at a critical temperature T_c is predicted (2). Such a blocking is probably caused by the formation of MRO with lifetimes that are long enough to generate vibrational motions. This interpretation is consistent with the observation that the temperature at which overdamping of the low-frequency vibrations occurs is essentially the same as the T_c predicted by the MCT (21). Although the boson peak tends to become dominant with decreasing temperature below T_c, the fast β-relaxation process persists. This is so because the intermolecular translational motions of each glycerol molecule can be overdamped even on a time scale of $\sim 10^{-12}$ s. If the system is rapidly quenched, the configuration of the MRO will be preserved to form a metastable glass phase, whereas if it is cooled very slowly, the locally stable MRO will be reorganized, resulting in the thermodynamic phase transition or crystallization (22).

The above model can be applied not only to the present molecular system but also to strong glass formers [in Angell's classification (23)] such as SiO_2 and B_2O_3 glasses. We recently carried out ab initio molecular orbital calculations on the clusters that model the MRO in B_2O_3 glass and have shown that these model clusters also yield localized vibrational modes in the low-frequency region, in good accord with experimental results (24).

REFERENCES AND NOTES

1. See, for example, C. A. Angell, Science 267, 1924 (1995); F. H. Stillinger, ibid., p. 1935; B. Frick and D. Richter, ibid., p. 1939.
2. W. Götze, in Liquids, Freezing, and the Glass Transition, J. P. Hansen, D. Levesque, J. Zinn-Justin, Eds. (North-Holland, Amsterdam, 1991), p. 287.
3. M. Krüger, M. Soltwisch, I. Petscherizin, D. Quitmann, J. Chem. Phys. 96, 7352 (1992); Z. Pan, D. O. Henderson, S. H. Morgan, ibid. 101, 1767 (1994); V. N. Novikov, E. Duval, A. Kisliuk, A. P. Sokolov, ibid. 102, 4691 (1995).
4. C. H. Wang and R. B. Wright, ibid. 55, 1617 (1971).
5. V. Z. Gochiyaev, V. K. Malinovski, V. N. Novikov, A. P. Sokolov, Philos. Mag. B 63, 777 (1991).
6. E. Rössler, A. P. Sokolov, A. Kisliuk, D. Quitmann, Phys. Rev. B 49, 14967 (1994); S. Kojima, ibid. 47, 2924 (1993).
7. J. Wuttke et al., Phys. Rev. Lett. 72, 3052 (1994); F. Fujara, W. Petry, R. M. Diehl, W. Schnauss, H. Sillescu, Europhys. Lett. 14, 563 (1991).
8. S. Kojima, J. Mol. Struct. 294, 193 (1993).
9. M. Garawi, J. C. Dore, D. C. Champeney, Mol. Phys. 62, 475 (1987).
10. N. Pugliano and R. J. Saykally, Science 257, 1937 (1992); M. Schütz, T. Bürgi, S. Leutwyler, H. B. Bügi, J. Chem. Phys. 99, 5228 (1993); S. S. Xantheas and T. H. Dunnin Jr., ibid. 98, 8037 (1993).
11. F. Huisken and M. Stemmler, Chem. Phys. Lett. 144, 391 (1988); O. Mó, M. Yáñez, J. Elguero, J. Mol. Struct. (Theochem.) 314, 73 (1994).
12. D. Peeters and G. Leroy, J. Mol. Struct. (Theochem.) 314, 39 (1994).
13. As the MRO in glycerol, much larger structures such as the cyclic tetramer and pentamer are also probable; but in this work we concentrated on the vibrational properties of the cyclic trimer. Even if such larger structures are present in real liquids, our general observations and conclusions should remain valid.
14. W. J. Hehre, R. Ditchfield, J. A. Pople, J. Chem. Phys. 56, 2257 (1972).
15. M. J. Frisch et al., Gaussian 94, Revision B 3 (Gaussian Inc., Pittsburgh, 1995).
16. In the strict sense, the trimer has a C_1 structure. We have confirmed that the total energy obtained for the present optimized cluster is lower than that calculated for the cluster assuming an ideal C_3 symmetry.
17. The energy obtained (-172.48 kJ mol^{-1}) is almost twice that calculated for the methanol trimer at the same level of theory [-92 kJ mol^{-1} (10)]. This is not surprising because the number of intermolecular hydrogen bonds in the glycerol trimer is six, whereas that in the methanol trimer is three.
18. P. Pulay, Mol. Phys. 17, 197 (1969).
19. M. J. Frisch, Y. Yamaguchi, J. F. Gaw, H. F. Schaefer III, J. S. Binkley, J. Chem. Phys. 84, 531 (1986).
20. W. J. Hehre, L. Radom, P. v. R. Schleyer, J. A. Pople, Ab Initio Molecular Orbital Theory (Wiley, New York, 1986), p. 233.
21. A. P. Sokolov, A. Kisliuk, D. Quitmann, A. Kudlik, E. Rössler, J. Non-Cryst. Solids 172–174, 138 (1994).
22. The structures and energies of molecular oligomers abstracted from their crystal structures are, in general, not expected to be optimum for the isolated oligomers [see, for example, D. E. Williams and Y. Xiao, Acta Crystallogr. A49, 1 (1993)].
23. C. A. Angell, J. Phys. Chem. Solids 49, 863 (1988).
24. T. Uchino and T. Yoko, J. Chem. Phys., in press.
25. We thank the Supercomputer Laboratory, Institute for Chemical Research, Kyoto University, for providing the computer time and for permission to use the Cray Y-MP2E/264 supercomputer.

Crystalline Ropes of Metallic Carbon Nanotubes

Andreas Thess, Roland Lee, Pavel Nikolaev, Hongjie Dai, Pierre Petit, Jerome Robert, Chunhui Xu, Young Hee Lee, Seong Gon Kim, Andrew G. Rinzler, Daniel T. Colbert, Gustavo E. Scuseria, David Tománek, John E. Fischer, Richard E. Smalley*

Fullerene single-wall nanotubes (SWNTs) were produced in yields of more than 70 percent by condensation of a laser-vaporized carbon-nickel-cobalt mixture at 1200°C. X-ray diffraction and electron microscopy showed that these SWNTs are nearly uniform in diameter and that they self-organize into "ropes," which consist of 100 to 500 SWNTs in a two-dimensional triangular lattice with a lattice constant of 17 angstroms. The x-ray form factor is consistent with that of uniformly charged cylinders 13.8 ± 0.2 angstroms in diameter. The ropes were metallic, with a single-rope resistivity of <10^{-4} ohm-centimeters at 300 kelvin. The uniformity of SWNT diameter is attributed to the efficient annealing of an initial fullerene tubelet kept open by a few metal atoms; the optimum diameter is determined by competition between the strain energy of curvature of the graphene sheet and the dangling-bond energy of the open edge, where growth occurs. These factors strongly favor the metallic (10,10) tube with C_{5v} symmetry and an open edge stabilized by triple bonds.

Carbon nanotubes, originally discovered as a by-product of fullerene research (1, 2), are attracting increasing interest as constituents of novel nanoscale materials and device structures (3). Defect-free nanotubes—essentially, giant linear fullerenes—are expected to have remarkable mechanical properties, as well as electronic and magnetic properties that are in principle tunable by varying the diameter, number of concentric shells, and chirality of the tube (4). Further progress toward the use of

nanotubes as practical materials will require the elimination of defects and other reaction products (such as amorphous carbon and catalyst particles), production in high yield, and synthetic control of tube diameter, length, chirality, and number of concentric shells.

SWNTs have been produced in the outflow of a carbon arc (2, 5) and in much higher yield by laser vaporization of a graphite rod in an oven at 1200°C (6); in each case, a small amount of transition

metal was added to the carbon target. We have optimized the laser-oven method further to produce SWNT yields of >70% (7). Here, we use x-ray diffraction (XRD) and transmission electron microscopy (TEM) to show that these SWNTs are remarkably uniform in diameter and that they self-organize into ropelike crystallites 50 to 200 Å in diameter and tens to hundreds of micrometers long. The crystallites form a two-dimensional (2D) triangular lattice, with lattice constant $a = 17$ Å, through van der Waals intertube bonding. These ropes are metallic, and we argue that a particular tube, (10,10) (4), may be the dominant component.

High-purity samples of SWNT consist of a mat of randomly oriented SWNT fibers 10 to 20 nm in diameter and many micrometers long (Fig. 1A). A typical TEM image of material deposited from a drop of a well-sonicated sample of 1 to 2 mg of the raw mat in 5 ml of methanol (Fig. 1B) shows that it consists primarily of bundles of SWNTs, or ropes, in which the SWNTs are aligned except for occasional branching and maintain a constant rope diameter over the entire length. In some TEM views, we have observed ropes longer than 100 μm. A TEM view of a rope as it curves through the field of view (Fig. 1C) illustrates the highly uniform SWNT diameter that is typical of these ropes (from Fig. 1C, the lattice constant is estimated to be ~17 Å).

None of our TEM images revealed any multiwall nanotubes (MWNTs). We estimate that 70 to 90% of the material typically consists of SWNT ropes. In the runs that produced the highest yields, we did not find the end of a rope in a TEM image. When only a single laser was used to evaporate the graphite rod, the yield was typically 50 to 60% and rope ends could be found. Remarkably, in these samples the individual SWNTs within any rope were found to terminate at the end of the rope within a few nanometers of each other. With very rare exceptions (<1 in 1000), each SWNT appeared to be continuous and free of defects. We found many examples in which the SWNTs appeared to have eaten

their way through particles of apparently amorphous carbon. In the TEM images, the ends of all SWNTs appeared to be perfectly closed with hemispherical end caps, with no evidence of any associated metal catalyst particle. Ni-Co particles were randomly distributed through the material and were usually found to be embedded in largely amorphous carbon.

We performed XRD at 300 K in the flat-plate (reflection) geometry (8) on a 1 cm by 1 cm piece (~5 mg) cut from the mat, which readily adhered to an etched Si(111) wafer moistened with ethyl alcohol (Fig. 2A). The low-Q region is dominated by small-angle scattering, which is unsurprising in light of Fig. 1. A strong discrete peak occurs near $Q = 0.44$ Å^{-1} ($2\theta \sim 6°$), as do four weaker peaks (up to $Q = 1.8$ Å^{-1}) that are consistent with the 2D triangular lattice. A small, sharp peak occurs at 1.85 Å^{-1}, which is very near the graphite(002) position; the XRD profiles of MWNTs are dominated by this reflection (9, 10).

Notably absent is the graphite(100) expected at $Q = 2.95$ Å^{-1}, which is observed in MWNTs with a line shape perturbed by the curvature of the graphene sheets (9). Evidently, the more severe curvature of

our smaller SWNTs broadens the (hk0) reflections to such an extent that they are no longer detectable. The sizable background in Fig. 2A comprises air scattering (dominant below 2 Å^{-1}), incoherent (Compton) scattering (independent of Q), and diffuse scattering from amorphous carbon. The important observation is that—apart from signatures of trace Co, Ni, and possibly MWNTs, carbon capsules, or graphite—the XRD profile, which averages over 5 mg of material, is dominated by Bragg peaks that are entirely consistent with the TEM images.

We analyzed the XRD data in detail by first fitting the entire profile to a sequence of discrete reflections of arbitrary line shape plus a polynomial background. We then subtracted the fitted background from the raw data (Fig. 2B, curve a). Our initial attempt to index the difference profile on a triangular lattice led to major discrepancies in several positions, which could not be satisfactorily accounted for even by considering a lower symmetry— namely, a centered rectangular lattice with $b/a \neq \sqrt{3}$ (11). This problem was resolved by the realization that the SWNT form factor is well approximated by the
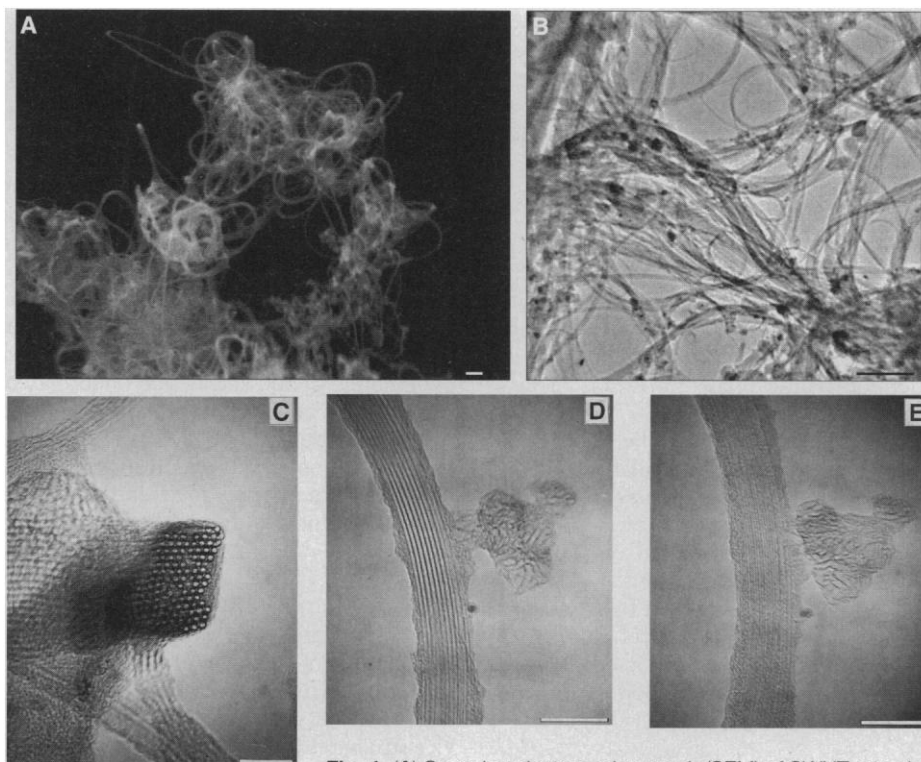
A. Thess, P. Nikolaev, H. Dai, C. Xu, A. G. Rinzler, D. T. Colbert, G. E. Scuseria, R. E. Smalley, Center for Nanoscale Science and Technology, Rice Quantum Institute, and Departments of Chemistry and Physics, Mail Stop 100, Rice University, Post Office Box 1892, Houston, TX 77251, USA.
R. Lee and J. E. Fischer, Department of Materials Science and Engineering and Laboratory for Research on the Structure of Matter, University of Pennsylvania, Philadelphia, PA 19104–6272, USA.
P. Petit and J. Robert, Institut Charles Sadron, 6 rue Boussingault, 67000 Strasbourg, France.
Y. H. Lee, S. G. Kim, D. Tománek, Department of Physics and Astronomy, Michigan State University, East Lansing, MI 48824–1116, USA.

*To whom correspondence should be addressed.

Fig. 1. (A) Scanning electron micrograph (SEM) of SWNT material, showing a mat of tangled carbon fibers 10 to 20 nm in diameter and many micrometers long. Scale bar, 100 nm. **(B)** At low resolution (scale bar, 100 nm), the material is shown to consist almost entirely of ropes of SWNTs, together with small amounts of metal catalyst particles coated with amorphous carbon. **(C)** A single SWNT rope made up of ~100 SWNTs as it bends through the image plane of the microscope, showing uniform diameter and triangular packing of the tubes within the rope. Scale bar, 10 nm. **(D** and **E)** Side views of a rope segment for two azimuthal orientations differing by 30°. Note the difference in fringe spacing (see text). Scale bars, 20 nm. The views in (B) through (E) are TEM images.

cylindrical Bessel function $J_o(QR)$, where R is the SWNT radius. Assuming no azimuthal correlations between SWNTs within a rope, this is analogous to using the spherical Bessel function $j_o(QR')$ to model the diffraction from orientationally disordered solid C_{60} (12), with one important difference. In C_{60}, the crystalline coherence length is large, so the XRD peaks are extremely sharp and j_o modulates only the observed intensities. The finite diameter of our rope crystals produces broad peaks [$\Delta(2\theta) \sim 0.5°$]. Moreover, the oscillations in J_o are spaced roughly twice as closely as in j_o, and R is about twice R', such that the diffraction widths observed in SWNT ropes are an appreciable fraction of the width of the lobes in J_o. Thus, J_o modulates the positions and shapes of the peaks as well as their intensities, so the lattice constant and tube diameter must be optimized simultaneously (shown in Fig. 2B, curve b, for a peak broadening of 0.5°). The vertical tick marks in curve b are the "infinite crystal" Bragg positions, which
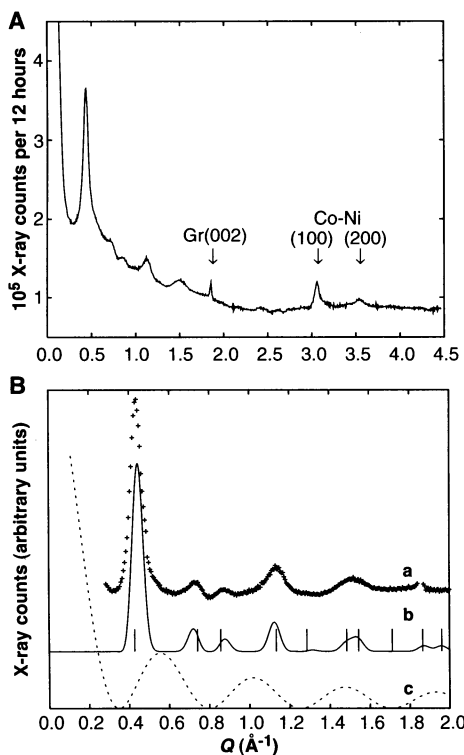
only coincide with the calculated maxima for reflections that happen to lie near peaks in J_o (Fig. 2B, curve c). The calculated profile is very sensitive to both a and R; deviations in either parameter lead to discrepancies in relative intensities, widths, and positions. We estimate the uncertainties as $\pm 2\%$ and $\pm 1.5\%$ for a and R, respectively. The van der Waals gap $(a - 2R)$ is 3.15 Å; this gap size, about the same as in solid C_{60} (12), is 0.3 Å less than the turbostratic limit for graphite and is consistent with a calculation for a lattice of somewhat smaller SWNTs (13). Apparently, the interaction between tubes 13.8 Å in diameter is not sufficiently strong to distort their cylindrical shape, as was predicted to occur for tube diameters exceeding 15 to 20 Å (14). The observed peak width yields a coherence length of ~ 100 Å, which is consistent with the diameters of the ropes observed in the TEM images.

The observation of well-defined 2D lattice reflections confirms that the SWNT diameter is highly uniform. Random diameters would produce paracrystalline disorder because of fluctuations in the lattice constant and in $\Delta(2\theta)$, so peak widths would increase as some power of Q. Two or more discrete diameters would likely produce a phase separation and a superposition of lattices with different lattice constants. Evidence that the 2D triangular lattice persists along a substantial length of rope is provided by TEM (Fig. 1, D and E). We imaged a rope segment normal to its long axis and examined the lattice fringe spacing as a function of rotation about the rope axis. The observed spacing decreases from 15.03 to 8.53 Å as the sample is rotated 30°. If we assume that these values represent views along the [1,0] and [1,1] axes, respectively, then $a = (\sqrt{3}/2)\, d_{[1,0]} = 17$ Å (in agreement with the value from XRD) and $d_{[1,0]}/d_{[1,1]} = 1.76$ (consistent, within experimental accuracy, with the value $\sqrt{3}$ required by trigonal symmetry).

We directly measured the electrical re-

sistivity (ρ) of a single rope by a four-point technique (15). In three separate experiments with different ropes, linear current-voltage curves were observed, with good stability (Fig. 3). The calculated resistivity of these ropes ranged from 0.34×10^{-4} to 1.0×10^{-4} ohm·cm. The principal error source here was estimation of the rope diameters from TEM; upper limits were used. The intrinsic axial resistivity ($\rho_\parallel$) of an individual SWNT in one of these ropes may be considerably less than the value indicated by this simple four-point measure because the tube-tube resistivity ($\rho_\perp$) may be $>10^4 \, \rho_\parallel$, as it is in graphite, and the ropes we measured may not have been long enough to ensure that only $\rho_\parallel$ was being measured. However, the value of 0.34×10^{-4} ohm·cm already indicates that these ropes are the most highly conductive carbon fibers known (16) and that their ρ values are about an order of magnitude lower than the lowest ρ yet measured for a MWNT (17).

Our first attempt to observe metallic behavior by means of electron spin resonance (ESR) was complicated by the presence of the ferromagnetic catalyst residues, which produced an intense line with a linewidth $\Delta H \sim 400$ G at 300 K. Vacuum-annealing at 1500°C eliminated this line as well as the XRD peaks characteristic of Co-Ni, and the sample was not attracted to a permanent magnet. We observed only a narrow Dysonian line with a Landé factor $g = 2.001 \pm 0.001$; this value is characteristic of a metal for which the skin depth (at 10 GHz) is less than the sample dimensions (Fig. 4). For comparison, polycrystalline graphite exhibits a line that is typical of a powder spectrum with an anisotropic g factor ($g_\parallel = 2.035$ and $g_\perp = 2.009$), whereas a sample of amorphous carbon derived from coal pitch gives a symmetric (non-Dysonian) line near $g = 2$ with a peak-to-peak linewidth $\Delta H_{pp} = 40$ G. The only previous ESR measurement on oriented MWNT (18) yielded a symmetric line whose temperature dependence and magnitude and

Fig. 2. XRD profile of SWNT material from the same batch as shown in Fig. 1 (7). (**A**) Raw data (total counts versus $Q = 4\pi \sin\theta/\lambda$). Gr, graphite. (**B**) Data-fitted background (curve a) compared with a model profile (curve b) that assumes a 2D triangular lattice of uniformly charged cylinders, $a = 16.95$ Å, and circle radius = 6.9 Å. Vertical tick marks on curve b are the calculated Bragg positions. Curve c shows how the square of the Bessel function form factor $J_0(QR)$ distorts the broadened reflections in position and shape, in addition to modulating the intensities.

Fig. 3. Optical microscope view (magnification ×800, numerical aperture 0.65) of four-probe measurement of the resistivity of a single SWNT rope, next to a diagram of the procedure (the boxed area corresponds to the image). A small piece of raw SWNT mat is clamped to a manipulator (right). A sharpened Pt tip (left), previously coated with a 10-nm layer of acrylic polymer adhesive, is driven a few micrometers into the mat and is then pulled out (to the position shown) to extract a single SWNT rope that remains attached to the mat (right). Two MWNT probes (top) reach in and make contact with the rope; these probes allow measurement of the voltage drop across this central region of the rope as a current (0.1 to 1 μA) is run along the tube between the mat and the Pt electrode.
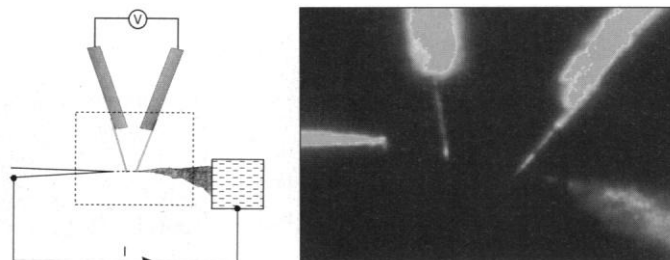
anisotropy of g were consistent with those of small, graphite-like semimetallic particles.

The yield of SWNTs from the optimized laser-oven production method is so high, and the degree of uniformity in diameter is so pronounced, that most nucleation and growth mechanisms that come to mind are clearly inadequate. For example, the production of SWNTs from a Ni-Co cluster of the correct size (19), in direct analogy to the well-known metal-catalyzed production of multiwalled fullerenes (20) and carbon fibers (21), requires metal clusters to form rapidly enough in these laser-oven conditions to serve as nuclei for growth and requires that all of these metal clusters be precisely the correct size to form a SWNT 13.8 ± 0.2 Å in diameter (22). Similarly, the recent suggestion that the nucleating species is a C_{10} to C_{40} polyyne ring interacting with a $Co_m C_n$ catalyst particle (23) seems incapable of explaining the high uniformity of these laser-oven–produced SWNT ropes.

We hypothesize a "scooter" mechanism as the most likely explanation for our yield and uniformity results (24). In this mechanism, the SWNTs are produced as an offshoot of the process that otherwise produces C_{60} in high yield. Initially, a single Ni or Co atom chemisorbs to the open edge of a curving graphene sheet, C_n, where $n \leq 50$. If the metal atom is bound sufficiently well (>2 eV) to this edge, then it will stay chemisorbed at 1200° to 1500°C for $\geq 10^{-8}$ s until another atom from the Ni-Co atomic vapor (density $\sim 10^{15}$ atoms cm^{-3}) hits, accommodates, and migrates to take its place. The metal atom must have a sufficiently high electronegativity that it avoids formation of an endohedral fullerene (25), and it must be highly effective in catalyzing the rearrangement of carbon rings. If the barrier to diffusion of this metal atom is sufficiently small (≤ 1 eV), the atom will "scoot" around the open edge of the sheet, helping to anneal away any carbon structures that are not the most energetically favored.
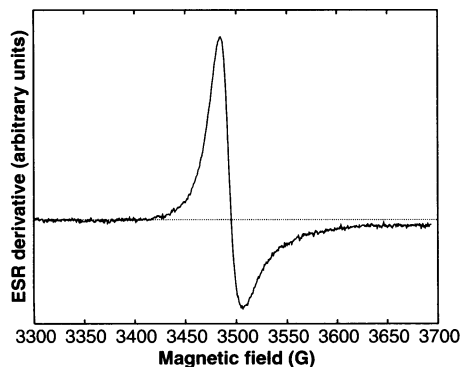
Attempts to identify the most favored structures for the scooter mechanism have made use of extensive tight binding (TB) (26) and local density functional calculations (27). These calculations have revealed that a key structural feature is the ability of the open edge of a curving graphene sheet to tie up its dangling bonds by forming strained triple bonds along the periphery (28). For a carbon cluster of 20, 30, 40, or 50 atoms, this can best be achieved by arranging pentagons and hexagons so that the periphery of the cluster is in the armchair configuration, with only the sides of the polygons exposed and all two-coordinated atoms arranged in triply bonded pairs. The optimized bond length of these paired atoms is 1.23 to 1.26 Å, near the normal triple-bond length, and the energy advantage of this configuration compared with the alternative zigzag edge is in the range of 0.8 eV per two-coordinated atom. On the C_{30} open cap-shaped cluster with C_{5v} symmetry, the optimum binding site for a Ni atom is above the "seat" of the armchair, forming a five-membered ring with a binding energy of 2.5 eV. Our preliminary estimate for the diffusion barrier to the next most favored site above the triple bonds is 1 eV, which supports the notion that a Ni atom will be an effective scooter at 1200°C.

A curving graphene sheet with a fully triply bonded armchair open edge can only contain six pentagons. Adding the 7th through 11th pentagons cannot be done without introducing a portion of zigzag edge, with an energy cost of at least 0.8 eV per zig atom. In addition, the pentagons themselves have an energy cost compared with the alternative hexagons that would begin to form a straight tube, and the added strain of curvature is also a factor (29). Therefore, there is always a barrier to the closure of a hemifullerene cap or tubelet; this kinetic impediment to the formation of a closed fullerene is similar to the problem of building a dome without a keystone. In the absence of a metal catalyst, this barrier is routinely overcome because incoming carbons can stay locked in

locally nonoptimum structures until enough carbon has come in to bridge the gap. A metal-atom scooter promptly anneals these local structures into hexagons, lengthening the straight tube section and keeping the end of this tubelet completely open.

The optimum initial tubelet kept open at its end by a scooter atom would be of the diameter of C_{60}. However, the strain energy per atom for curving a graphene sheet into a cylinder is quite high at this small diameter. If the temperature is high enough and the growing tube is still small enough to rearrange to its most favored form, it will readjust to form a tube that has a larger diameter but still has its open-edge energy reduced by triple-bond formation as much as possible. The Ni and Co atoms diffusing over the surface of the growing tubelet [and small carbon radicals as well (30)] may help to catalyze these massive rearrangements. At some size (N_{crit}), however, the tubelet finally has too many atoms to rearrange on the relevant time scale. It becomes kinetically locked forever at this particular diameter and helicity, even though it may continue to grow thousands of times as long.

Extensive TB calculations for a wide range of tubelets (24, 31) show that this scooter mechanism can explain our experimental results. For tubelets that become locked in the critical size range of 250 to 600 atoms, the most energetically favored tube is (10,10). A model of a tubelet leading to this (10,10) tube, just after it has grown into this critical size range, is shown in Fig. 5. Below $N_{crit} = 250$, the (9,9) and (8,8) tubes become favored; above $N_{crit} = 600$, the (12,12) tube begins to be the lowest in energy. All of these tubes are zero-helicity armchair tubes (32) that are predicted to be metallic and to have the highest stiffness of any helicity (29). The (10,10) tube is estimated by TB (24) to have a diameter of 13.6 Å, which is consistent (within experimental error) with the XRD and TEM results.

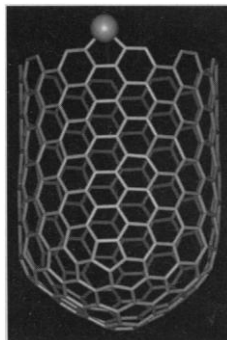The formation of 2D crystalline ropes of SWNTs can be understood as a result of

Fig. 4. The 300 K ESR spectrum (10 GHz) of SWNT material vacuum-annealed at 1500°C.

Fig. 5. View of the critical nucleus of a (10,10) SWNT with a Ni atom chemisorbed onto the open edge. The Ni (or Co) atom keeps the tube open by scooting around the open edge and ensuring that any pentagons or other high-energy local structures are rearranged to hexagons. The tube shown has 310 atoms. This (10,10) tubelet is energetically preferred over all others in the size range from 250 to 600 atoms. If we assume that the growing clusters do not have time to rearrange to a larger diameter tube by the time they have grown this large, the (10,10) tube will be the dominant SWNT in the final material. Later in the growth process, more metal atoms congregate at the open (live) end, forming a catalytic Ni-Co cluster that is able to disassemble fullerenes and other large carbon species.

collisions between growing tubelets in the gas phase, while they are still short enough to align by van der Waals forces without becoming tangled. Feedstock for the SWNT arrives at the "live" end, mostly by diffusion of carbon clusters along the sides of the tube. When a SWNT is in contact along the side of a longer rope, it receives additional feedstock diffusing down the rope from the front, and its growth accelerates until it catches up with the longest SWNT in this direction of the rope (which is growing more slowly because it can only receive feedstock from the rear). Although only a single atom need be involved in the original nucleation and early growth of a SWNT, other metal atoms will soon congregate at the live end, forming a small metal cluster. Later in the growth process, the carbon feedstock will primarily be in the form of fullerenes and other large carbon aggregates. The Ni-Co mixed-metal catalyst that exists at the live end of the growing nanotubes at this stage can efficiently dismantle these large carbon species, digesting them into atoms or small radicals that can diffuse to the growing edge of the SWNT. The metal cluster ultimately leaves the end of the SWNT either by evaporation or, if the cluster is sufficiently large (33), by slowly catalyzing the closure of the SWNT with a hemi-fullerene dome.

REFERENCES AND NOTES

1. S. Iijima, *Nature* **354**, 56 (1991).
2. _____ and T. Ichihashi, *ibid.* **363**, 603 (1993); D. S. Bethune *et al.*, *ibid.*, p. 605.
3. L. Chico, V. H. Crespi, L. X. Benedict, S. G. Louie, M. L. Cohen, *Phys. Rev. Lett.* **76**, 971 (1996).
4. M. S. Dresselhaus, G. Dresselhaus, P. C. Eklund, *Science of Fullerenes and Carbon Nanotubes* (Academic Press, San Diego, 1996).
5. P. M. Ajayan *et al.*, *Chem. Phys. Lett.* **215**, 509 (1993).
6. T. Guo, P. Nikolaev, A. Thess, D. T. Colbert, R. E. Smalley, *ibid.* **243**, 49 (1995).
7. Samples were prepared by laser vaporization of graphite rods doped with 1.2 atomic % of a 50:50 mixture of Co and Ni powder (particle size ~1 μm) at 1200°C in flowing argon at 500 torr, followed by heat treatment in vacuum at 1000°C to sublime out C_{60} and other small fullerenes. As an improvement over the method described previously (6), the initial laser vaporization pulse (532 nm, 250 mJ in a 5-mm-diameter spot at 10 Hz) was followed 50 ns later by a second pulse (1064 nm, 300 mJ in a 7-mm-diameter Gaussian spot coaxial with the first laser) to provide more uniform vaporization of the target [G. Koran, R. J. Baseman, A. Gupta, M. I. Lutwyche, R. B. Laibowitz, *Appl. Phys. Lett.* **56**, 2144 (1990); S. Witanachchi and P. Mukherjee, *J. Vac. Sci. Technol. A* **13**, 1171 (1995)].
8. The diffractometer was a sealed Cu tube (wavelength λ = 1.54 Å) operating at 1 kW, with a flat graphite(002) monochromator, a fixed sample angle at grazing incidence, and a linear detector (radius 25 cm) that allowed parallel accumulation of 4096 channels covering 120° in 2θ. We assumed no preferred orientation of the rope crystallites, which was a concern because our flat-plate diffractometer had no provision for rotating the sample during data collection. Two observations convinced us that the rope axes were indeed randomly oriented within the mat: (i) We compared flat-plate profiles collected at several incident angles and found no difference in relative intensities. (ii) We measured a profile from a spinning capillary sample (Debye-Scherrer geometry) and again found relative intensities similar to those from the flat plate, albeit with a poorer signal/noise ratio because of the smaller scattering volume and the additional diffuse scattering from the capillary.
9. O. Zhou *et al.*, *Science* **263**, 1744 (1994); D. Reznik, C. H. Olk, D. A. Neumann, J. R. D. Copley, *Phys. Rev. B* **52**, 116 (1995).
10. We identified peaks at 3.06 and 3.54 Å⁻¹ with (111) and (200) reflections of Co-Ni, which persist after annealing at 1000°C as crystallites with an average size of 120 Å. The integrated intensity of "graphite(002)" is at least an order of magnitude lower, indicating <0.1 atomic % carbon as MWNTs or capsules (which were apparently eliminated from the TEM specimens) or possibly as adventitious graphite from the target. Very weak reflections in the range Q = 2.0 to 3.0 Å⁻¹ can also be indexed on the triangular lattice.
11. We envisioned several reasons why the sixfold rotational symmetry might be broken: (i) two closely spaced tube diameters; (ii) curvature of the ropes (evident from the TEM micrographs); or (iii) frustration of triangular close packing if the symmetry of the dominant SWNT is incompatible with sixfold rotation [such as the (10,10) tube with C_{5v} symmetry].
12. P. A. Heiney, *J. Phys. Chem. Solids* **53**, 1333 (1992).
13. J.-C. Charlier, X. Gonze, J.-P. Michenaud, *Europhys. Lett.* **29**, 43 (1995).
14. J. Tersoff and R. S. Ruoff, *Phys. Rev. Lett.* **73**, 676 (1994).
15. A single rope was attached to a sharpened Pt electrode and pulled out from a tangle of the raw SWNT mat material. Under an optical microscope (magnification ×800), a current of 0.1 to 1 μA was run along the rope by connection of opposite poles of a stable dc current source to wires leading to the Pt electrode and the mat. The voltage drop along the SWNT rope was then measured between two arc-grown MWNTs mounted on carbon fibers [A. G. Rinzler *et al.*, *Science* **269**, 1550 (1995)] and positioned into contact on the side of the SWNT rope at a measured distance of 5 to 10 μm. The rope was then imaged directly by TEM to determine its diameter.
16. M. S. Dresselhaus, G. Dresselhaus, K. Sugihara, I. L. Spain, H. A. Goldberg, in *Graphite Fibers and Filaments*, M. Cardona *et al.*, Eds., vol. 5 of Springer Series in Materials Science (Springer-Verlag, New York, 1988), pp. 188–202.
17. H. Dai, E. W. Wong, C. M. Lieber, *Science* **272**, 523 (1996). We also measured ρ (at 300 K) for an unoriented piece of mat (1.2 cm by 0.25 cm) by pressing it against a microscope slide with four silver foil contacts (0.4 cm between voltage probes). The resistance was 21 ohms. On the basis of a microscopic thickness determined from the length, width, and measured mass (150 μg), and an assumed microscopic density of 2 g cm⁻³, we estimated a directionally averaged bulk resistivity intermediate between the resistivities of C_{60} and graphite. This estimate, 3 × 10⁻³ ohm·cm, is less than two orders of magnitude greater than the single-rope value of $\rho_\parallel$ reported above and provides further evidence that the ropes within the mat material are continuous for hundreds of micrometers. Moreover, the mat measurement yielded a positive temperature derivative $d\rho/dT$ near 300 K, a definitive sign of metallic behavior. In contrast, a recent measurement of an individual MWNT shows thermally activated conductance (negative $d\rho/dT$) [L. Langer *et al.*, *Phys. Rev. Lett.* **76**, 479 (1996)].
18. O. Chauvet *et al.*, *Phys. Rev. B* **52**, R6963 (1995).
19. We recently produced SWNTs 0.7 to 3 nm in diameter with preformed Ni-Co metal particles on a fumed alumina support from a CO reactant gas at 1 atm and 1100°C [H. Dai *et al.*, in preparation]. Each of these SWNTs was found to have a metal particle at its tip, with a diameter appropriate to the tube it catalyzed.
20. S. Amelinckx *et al.*, *Science* **265**, 635 (1994).
21. G. G. Tibbetts, in *Carbon Fibers, Filaments and Composites*, J. L. Figueiredo *et al.*, Eds. (Kluwer Academic, Amsterdam, 1990), pp. 73–94.
22. Metal particles of adequate size are made too late in the condensation process. In the case of our double laser vaporization technique, there is little question that the metal is quite effectively atomized and mixed with the carbon in the vapor. In such a carbon-dominated vapor, the carbon clusters will begin to form first, and the metal then starts to condense atom-by-atom onto the surface of these carbon aggregates. Metal clusters near 13.6 Å in diameter will contain >100 atoms, by which time the average carbon cluster will contain >10⁴ atoms.
23. C.-H. Kiang and W. A. Goddard III, *Phys. Rev. Lett.* **76**, 2515 (1996).
24. A more extensive discussion of the scooter mechanism is forthcoming (C. Xu, D. T. Colbert, G. Scuseria, R. E. Smalley, in preparation).
25. T. Guo, R. E. Smalley, G. Scuseria, *J. Chem. Phys.* **99**, 352 (1993).
26. C. H. Xu, C. Z. Wang, C. T. Chan, K. M. Ho, *J. Phys. Cond. Matter* **4**, 6047 (1992).
27. Y. H. Lee, M. S. Kim, D. Tománek, unpublished results.
28. The edge energy of a carbon nanotube of helicity indices (a,b) and diameter $D = 0.78(a^2 + ab + b^2)$ is roughly
$$E_e = (\varepsilon_{db}N_{db} + \varepsilon_{tb}N_{tb})$$
where $N_{db} = a - b$ is the number of two-coordinated edge atoms that have a dangling bond, and $N_{tb} = 2b$ is the number of two-coordinated edge atoms that are involved in triple bonds. Rough estimates for the dangling-bond (db) and triple-bond (tb) energies per atom are ε_{db} = 2.9 eV and ε_{tb} = 2.1 eV from TB calculations (24) and ε_{db} = 2.8 eV and ε_{tb} = 2.0 eV from local density functional calculations (27). Zero-helicity armchair tubes are those with $a = b$.
29. D. H. Robertson, D. W. Brenner, J. W. Mintmire, *Phys. Rev. B* **45**, 12592 (1992); P. W. Fowler and D. E. Manolopoulos, *An Atlas of Fullerenes*, vol. 30 of International Series of Monographs on Chemistry (Clarendon, Oxford, 1995).
30. B. R. Eggen *et al.*, *Science* **272**, 87 (1996).
31. The energy of an open-ended tubular fullerene, with six pentagons in a hemispherical cap at one end connected to a straight section, is
$$\Delta E = E_c + E_t + E_e$$
where E_c is the strain energy of the hemifullerene end cap, E_t is the strain energy of the tube wall ($E_t \approx \varepsilon_t L/D$, where L is the straight length of the tube of diameter D and $\varepsilon_t \sim$ 10 eV), and E_e is the energy of the open tube edge [$E_e = \varepsilon_e \pi D$, where ε_e depends on the helicity indices (a,b)]. To a good approximation, E_c is independent of diameter, but for a fixed diameter it is quite sensitive to the relative positioning of the six pentagons in the end cap. For caps with isolated pentagons and smooth curvature approximating a sphere, $E_c \approx$ 20 eV. For zero-helicity armchair tubes ($a = b$), $\varepsilon_e \approx$ 1 eV Å⁻¹. Explicit calculation of all possible nanotubes shows that the C_{5v} symmetry tubelet leading to the (10,10) SWNT is the most favored in the region from 300 to 600 atoms. The (9,9) and (8,8) tubelets begin to be favored for N_{crit} < 300 atoms; the (5,5) tubelet is the most favored for N_{crit} < 100 atoms; and the (12,12) tube dominates when N_{crit} > 600 atoms.
32. Electron diffraction with probe electron beams (diameter 1 to 2 nm) on individual ropes of this laser-oven SWNT material shows that the dominant tubes in these ropes are zero-helicity armchair tubes (J. Cowley, unpublished results).
33. A. G. Rinzler *et al.*, *Electrochem. Soc. Proc.*, in press.